



Searching for the formation of TiO₂ mesoporous films with durable photoactivity by synergy of WO₃ and sodium using a simple sputtering and annealing process



Giin-Shan Chen*, Chiaohung Cheng

Department of Materials Science and Engineering, Feng Chia University, Taichung 40724, Taiwan

ARTICLE INFO

Article history:

Received 22 September 2013

Accepted 11 December 2013

Available online 25 December 2013

Keywords:

Anatase TiO₂

Sputter deposition

Photocatalyst

Mesoporous film

WO₃

ABSTRACT

The fabrication of anatase TiO₂ thin films with a mesoporous framework by template-directing sol–gel or microemulsion method has drawn considerable attention because of the compound's highly photocatalytic and superhydrophilic properties and its potential use in a wide variety of applications, such as self-cleaning and anti-fogging. In this study, thin films of TiO₂, coupled with a widely ranging amount of WO₃, are sputter deposited onto soda-lime glass, and the segregation of WO₃ by annealing, along with the alternation of their microstructures and underlying reaction mechanisms involving sodium, is examined. This research highlights a sputtering process to synthesize mesoporous anatase films with a refined, regular grain structure and controlled porosities, via the synergy of WO₃ and sodium to form a water-soluble sodium tungstate through a simple annealing process. In contrast to what is generally agreed that sodium contaminates TiO₂ photocatalysts, the films impacted by sodium exhibit exceptional durability and much better photoactivity than the undoped anatase films at degrading a hydrocarbon layer and giving a long-last super-wetting surface. The enhancement of the films' photocatalytic activity is elucidated by structural analysis and porosity identification.

© 2013 Elsevier B.V. All rights reserved.

1. Introduction

Titanium dioxide (TiO₂) has long been proved to be the most suitable photocatalyst for general catalysis applications, such as environmental de-pollution, sterilization, and water purification [1,2]. Apart from its photocatalysis properties, film-type TiO₂ also exhibits photoinduced hydrophilicity on its coating surface [3]. By utilizing these properties, new applications of TiO₂ thin films can be developed, including self-cleaning/anti-fogging glass and antibacterial ceramic tiles [4]. Immobilizing TiO₂ as a thin film on a solid substrate has an additional merit of eliminating the post-separation treatment of a slurry system, which is required for conventional powder photocatalysts. However, TiO₂ thin films generally exhibit lower photocatalytic activity than the corresponding powder materials due to their smaller specific surface area [5,6]. The introduction of porosity to TiO₂ thin films helps to remedy this problem.

A mesoporous thin-film material could be a highly effective photocatalyst since it possesses higher specific area to offer more active sites for catalytic reactions [7,8]. The synthesis of mesoporous TiO₂ thin films is not entirely new, and the traditional approach is based on polymer-assisted sol–gel process or micelle-templated

method [9,10]. Typically, a low-temperature solvent-extracting or thermal treatment is performed to remove the templating agents used to manipulate the formation of mesoporous structures. However, the resultant films generally have a weak photoactivity due to poor crystallinity; the films also readily suffer from mechanical degradation or peeling during prolonged operation, due to the gradual release of the pyrolytic residues or weak adhesion between the films and substrates [11–13]. Calcination at high temperatures—with the aim to enhance crystallinity, to drive out the residues, or to promote interfacial adhesion—could be problematic, as it causes a deterioration of photoactivity due to the collapse of the mesoporous framework or the transformation of anatase to rutile TiO₂ [14–16].

Soda-lime glass is currently the most widely used glass material in industry and architecture. If a highly durable mesoporous TiO₂ film with a long-lasting photoactivity can be coated on the soda-lime glass, it would be quite useful for self-cleaning or anti-fogging glass-based commodities. However, sodium in the soda-lime glass tends to diffuse into the TiO₂ films during thermal annealing, which then acts as (a) a recombination center that eliminates the photon-generated electron-hole pairs [17,18], (b) an agent that promotes the grain growth of the TiO₂ films [19,20], or (c) a retarding factor that inhibits the formation of anatase or reduce crystallinity [18,21,22]. To prevent the uptake of sodium ions deteriorating photocatalytic activity, the soda-lime glass is pre-coated with an SiO₂

* Corresponding author. Tel.: +886 4 2452 9008; fax: +886 4 2451 0014.

E-mail address: gschen@fcu.edu.tw (G.-S. Chen).

(or SiN_x) barrier layer or soaked in an HCl solution to exchange sodium ions [18,23–25].

Coupling TiO_2 with tungsten species in the form of lattice dopants, surface wolframyl groups, or WO_3 compounds has been extensively studied as a photocatalyst over the past decades and has demonstrated enormous potential in enhancing photoactivity [26–28]. However, none of the previous works examine the effect of the glass's sodium on the phase transformation and photoactivity of WO_3 -coupled TiO_2 films. There has also been no report on the synthesis of mesoporous TiO_2 films directly from the $\text{TiO}_2/\text{WO}_3/\text{Na}$ ternary systems. We have recently examined the effects of annealing and the types of substrates (sodium-free and soda-lime glass slides) on the structural evolution and photocatalytic activity of sputter-deposited TiO_2 films, incorporating the same amount of WO_3 [29]. In contrast to what is generally agreed that sodium contaminates TiO_2 photocatalysts, that research has found that annealing causes the expulsion of WO_3 only from film coated on soda-lime glass. The resulting film is anatase-based and is superior to a rutile-based film in dissociating hydrocarbon molecules.

In this work, soda-lime glass slides will be used as substrates for the sputter deposition of TiO_2 films coupled with a widely ranging amount of WO_3 . The aim of this work is to elucidate further the underlying reaction mechanisms regarding the anneal-induced microstructural changes of the various films impacted by the glass's sodium. A new synthesis process via synergy of WO_3 and sodium through a simple sputtering and annealing process to form mesoporous anatase films with controlled porosities will be reported, and their photoactivity will be compared with the undoped anatase films: the well-known efficient photocatalysts. As is well-known, sputter deposition is a powerful and facile process tool, providing nonthermal energy input (as distancing from sol-gel or thermal evaporation methods) to process films with enhanced reliability and interfacial adhesion [30]. The mesoporous films indeed are highly durable and effective photocatalysts in degrading a hydrocarbon layer, and lend a long-lasting super-wetting surface, even much better than the undoped anatase films.

2. Experimental

2.1. Sample preparation

The catalytic films were deposited on soda-lime glass slides without intentional heating by poisoned-mode magnetron sputtering of commercially available 3 in. diameter Ti and Ti-W alloy targets (99.95% purity). The poisoned modes occurred in a reactive Ar-O_2 atmosphere with a total pressure of ~ 4 Pa, and were controlled by optical emission spectroscopy, which monitored the vanishing of Ti emission lines via a flow-supply feedback loop using a threshold oxygen flow rate [31]. Four film types were examined: undoped TiO_2 films from a Ti target; three doped TiO_2 films from Ti-W composite targets with pre-determined chemical compositions of Ti_{95}W_5 , $\text{Ti}_{90}\text{W}_{10}$, and $\text{Ti}_{75}\text{W}_{25}$. As measured by a high-precision step profilometer (ET3000, Kosaka Lab. Ltd.), thickness of all the films was 100 nm, with a variation of less than $\pm 2\%$. After deposition, all the film types were annealed in an oxygen-contained atmosphere (typically 550°C for 60 min), then washed in boiled water for a typical period of 10 s.

2.2. Composition analysis

The composition and the numbers of atoms per unit of surface area (areal densities) of titanium and tungsten for each film type were analyzed before and after the two-step processing

(annealing/water washing) by Rutherford backscattering spectroscopy (RBS) using a Van de Graaff accelerator. The samples were examined by a 2.0 MeV ^4He ion beam with normal incidence and the signals were detected at a backscattering angle of 170° . This data was determined with a $\pm 2.5\%$ accuracy by computer simulation of RBS spectra using a RUMP code. A Rutherford cross section for titanium was checked by measuring a reference sample with a known areal density.

Depth-profiling X-ray photoelectron spectroscopy (XPS) was performed to obtain the distributions of the elements across the samples, and particular attention was paid to the distributions of the segregated elements, i.e., tungsten and sodium. The spectrometer, Quantera SXMTM (ULVAC-PHI, Inc.), used monochromatized Al K_α radiation (1486.6 eV) as the X-ray source and an analytic chamber with a base pressure of less than 7×10^{-8} Pa. Argon ions accelerated by 1000 V were used for the depth profile analysis, bombarding a circular area ($\sim 1 \text{ mm}^2$) of the samples; the X-ray source was 45° from the sample surface. The hemispherical sector analyzer received the emitted photoelectrons by a constant-analyzer-energy mode.

2.3. Microstructural analysis

For every set of the samples, phase transition behaviors induced by the two-step processing were analyzed with grazing-incidence X-ray diffraction (XRD) using a synchrotron radiation source from the 17 B beamline at the National Synchrotron Radiation Research Center, Taiwan. The surface morphologies of the films, along with their fractured cross-sectional microstructures, were analyzed by high-resolution scanning electron microscopy (S-4800, Hitachi). An ultrahigh resolution analytic transmission electron microscope (JEM-2010F, JEOL), equipped with an energy dispersive X-ray (EDX) spectrometer (EMAX400, Horiba), was employed in key critical cases to characterize plan-views and cross sections of the films. The plan-view samples were prepared using a Precision Ion Polishing System (Model 691, Gatan, Inc., USA), which thinned the back side of the film-coated glass substrates until just perforation; cross-sectional samples were prepared by a focused ion beam system (SMI-3050SE, Seiko Instruments Inc.). The data collected allowed the segregation behavior among various sets of the samples to be distinguished and the porosity and crystalline structures of the featured samples to be identified.

2.4. Photocatalytic measurements

To evaluate photoactivities of the catalytic films, an octadecyltrichlorosilane [$\text{CH}_3(\text{CH}_2)_{17}\text{SiCl}_3$] self-assembled monolayer (OTS-SAM) was coated on the samples by the previously-mentioned process [32]. Next, the monolayer-coated samples were illuminated under ultraviolet light emitted from a mercury-vapor lamp, whose light intensity at 365 nm was 1 mW cm^{-2} . The SAM-coated samples were terminated by nonpolar methyl groups, and initially had a water contact angle of greater than 100° . The gradual decomposition of the nonpolar alkyl chains by photocatalytic oxidation led to a gradual decrease in water contact angle [33,34]. Hence, the photoactivity levels of the various catalytic films were evaluated by monitoring the evolution of the water droplet contact angles as a function of illumination time using an automatic contact-angle analyzer (FTA125, First Ten Angstroms, Inc., USA). In addition, the bare films were subjected to repeated cycles of ultraviolet illumination (1 day) and dark-room storage (1 day) for a period of about 3 months, and the activity and durability of their hydrophilicity were evaluated by using the water droplet method to measure their surface contact angles.

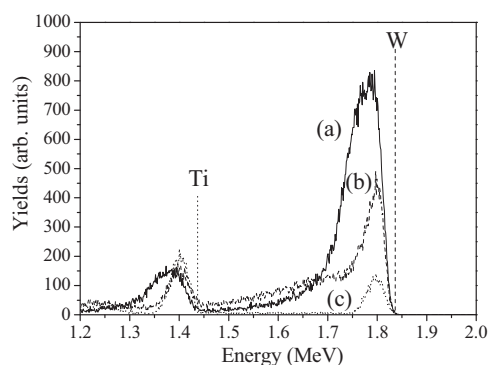


Fig. 1. A series of RBS spectra in the region of the Ti and W peaks typical of the heavily doped TiO_2 films (W/Ti atomic ratio = 0.55) before (a) and after the sequential treatments of annealing (b) and water washing (c). The vertical lines marked the high-energy edges of the two elements.

3. Results and discussion

3.1. Quantification of the processing-induced composition variations

First, RBS spectra for all of the as-deposited films were recorded. The areal densities of titanium and tungsten in the films were then determined by computer simulation, and a Rutherford cross section was checked for titanium by measuring a reference sample with a known areal density. These measurements showed that the W/Ti atomic ratio of each film type was higher than that of the alloy target: the W/Ti atomic ratios of the films prepared from Ti_{95}W_5 , $\text{Ti}_{90}\text{W}_{10}$, and $\text{Ti}_{75}\text{W}_{25}$ targets were 0.08, 0.14, and 0.55, respectively. As is well-known, compared to tungsten, titanium is easier to oxidize and also has a greater ability to capture oxygen. Under the conditions considered here, the poisoned titanium had a reduced value of sputtered flux, thus not giving sufficient titanium in the resulting films. Another reason for the deficiency of titanium was the difference in angular distributions of the sputtered flux arriving at the substrate: the lower atomic mass of titanium resulted in a greater average scattering angle with respect to that of tungsten during transport through the sputtering gas, resulting in a deficiency of titanium [35].

The impact of the two-step processing (annealing followed by water washing) on the alteration of the films' composition was monitored by RBS spectra, shown in Fig. 1, where the selected case of the film with an initial W/Ti atomic ratio of 0.55 can be seen. Initially, the peaks of titanium and tungsten were symmetrical at the positions defined, which was expected for the as-deposited film with uniform compositions (see spectrum a). As seen in spectrum b, annealing resulted in a skewing of the tungsten peak towards the low-energy region; the height and width of the peak were also significantly reduced. These changes suggest that some of the incorporated tungsten species were driven away from the film into the glass substrate. As seen in spectrum c of Fig. 1, a dramatic shrinkage of the tungsten peak occurred following the water washing. From the alternation of the integration yields under the tungsten peaks of the RBS spectra in Fig. 1, approximately 80% of the tungsten was removed from the film after the two-step processing. In contrast, the series of spectra in Fig. 1 shows that the two-step processing caused an increase in the height and a decrease in the width of the titanium peak due to a reduction in film thickness. However, the content of titanium, which was proportional to the area under the peak, was approximately constant, suggesting the absence of titanium segregation.

RBS spectra of other tungsten-incorporated films were recorded, after which the areal densities of their key constituents, titanium

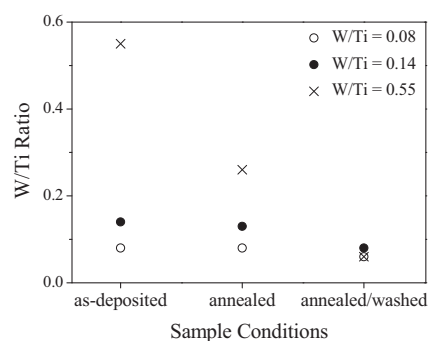


Fig. 2. Variations of W/Ti areal density ratios for the three tungsten-containing film types (W/Ti atomic ratios = 0.08, 0.14, and 0.55) as a function of the two-step processing.

and tungsten, were determined by simulation. Similarly, after the two-step processing, the areal densities of the titanium remained almost unchanged (within measurement errors), while those of the tungsten were reduced by a degree that was heavily dependent on the initial tungsten content. This can be seen from Fig. 2, which plots the areal density ratios of W to Ti as a function of the sample conditions. It should be noted that the W/Ti areal density ratios are independent of film thickness. Therefore, when examining the plots in Fig. 2, the behavior of tungsten loss from the films may be compared without compensating for the process-induced film thickness reductions. The reduction of W/Ti ratios of the films after annealing, shown in Fig. 2, was caused solely by the expulsion of tungsten species to the glass substrates. Moreover, the subsequent water washing caused a further drop in the tungsten content, the degree of which increased with the initial W/Ti ratios. For instance, a moderate reduction of ca. 20% occurred in the films with the initial W/Ti ratio of 0.08, while an extensive 90% loss of tungsten occurred in the films with the W/Ti ratio of 0.55. All of the films had a final, given specific amount of residual tungsten with a W/Ti ratio of approximately 0.07. XPS depth profiling and structural analyses (e.g., SEM and TEM) will be provided later to explain the loss of tungsten from the films.

The depth profiles of the sample films were further studied by XPS to understand the processing-induced segregation behavior. The concentration of sodium was difficult to analyze by RBS because its backscattering signals overlapped with the signals of some elements in the glass (e.g., Mg, Si, and Al). Therefore, the distributions of sodium across the depths of the samples were monitored. Depth profiles of the silicon were also recorded for interfacial identification. Selected results are shown in Fig. 3A–C for the films with an initial W/Ti ratio of 0.55. The plots in Fig. 3A demonstrate that the constituent elements (Ti, W, and O) were essentially confined and uniformly distributed within the as-deposited films. According to the depth profiling analysis, the degrees of segregation of sodium and tungsten both increased with the initial amounts of tungsten in the films. As revealed in Fig. 3B for the films after annealing, the segregation behavior was most apparent in the films with a W/Ti ratio of 0.55. First, tungsten with an atomic concentration level of ca. 3% was discovered within the underlying glass substrate, reinforcing the finding of the RBS analysis (Fig. 1). Second, tungsten was also expelled outwards, and then accumulated in the region near the free surface with increasing atomic concentrations of up to 18%; sodium within the glass was drawn out into the film and reached a substantial concentration level equal to that in the glass (~4%), gradually accumulating together with the tungsten, which also had increasing concentrations of up to ~20% near the free surface region.

Estimation from the depth profile of sodium in Fig. 3B reveals that the segregated sodium reached an average atomic

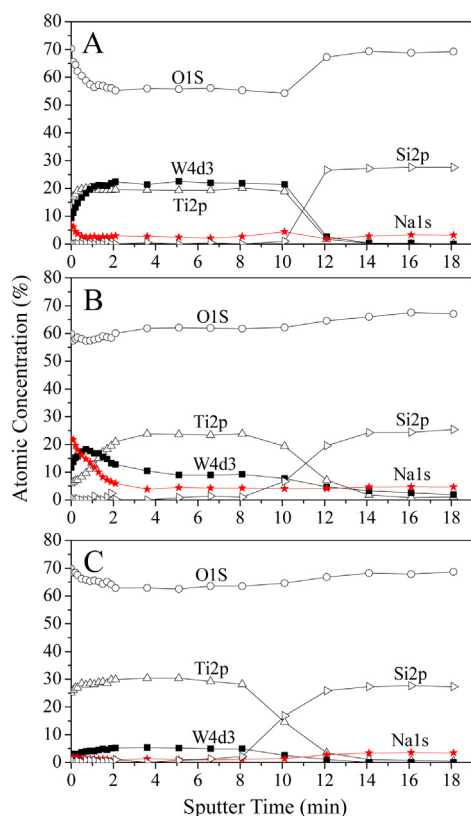


Fig. 3. XPS depth profiles obtained from the films (W/Ti atomic ratio=0.55) deposited on soda-lime glass before and after the two-step processing. (A): as-deposited sample; (B): annealed sample; (C) annealed/washed sample.

concentration level of 6.0% in the film (W/Ti ratio=0.55) after annealing. A related study (profile not shown) indicated that the anneal-induced segregation of sodium also occurred for films with reduced W/Ti ratios of 0.08 and 0.14; the average atomic concentration levels of sodium were 1.6 and 2.2%, respectively. This correlation indicates that the XPS depth profiling was supplemental to the RBS analysis, which suggests that the interplay between tungsten and sodium resulted in an extraction of the glass's sodium, as well as an outward segregation of tungsten. Moreover, the depth profiles in Fig. 3C reveal that after water washing, the concentration level of sodium subsequently dropped abruptly back to the background level and was accompanied by a further decay in the tungsten concentration level, an observation also found by the RBS analysis in Fig. 2.

3.2. Structural characterization

The findings presented so far suggest that the tungsten species has a high affinity and chemical reactivity with the sodium in the soda-lime glass substrates. Therefore, upon annealing, the two components mutually attract and then react with each other, forming a water-soluble substance. XRD, along with TEM, was performed to elucidate the phase transformation behavior. The results for the TiO_2 and all of the tungsten-incorporated films are summarized in the XRD patterns in Fig. 4, which shows that the pristine TiO_2 films that were deposited at a working pressure of 4 Pa only contained sharp peaks of anatase (JCPDS 21-1272) (pattern a). The formation of anatase here corresponds with the previous findings that TiO_2 molecules, formed under a high sputtering pressure of typically greater than 2 Pa, tend to coalesce on a substrate into an anatase phase, as they have a low surface mobility and thus are

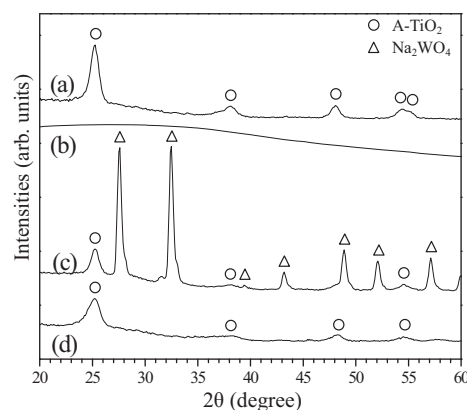


Fig. 4. XRD patterns typical of the TiO_2 -dominating samples (W/Ti=0, 0.08, and 0.14) with and without annealing (a), along with the patterns of the heavily-doped (W/Ti=0.55) TiO_2 samples before (b) and after the sequential treatments of annealing (c) and washing (d).

unable to combine into a thermodynamically favored rutile phase [36,37].

The as-deposited films (W/Ti ratio=0.08) yielded XRD patterns almost identical to those of the TiO_2 films (see pattern a, Fig. 4). The associated selected area electron diffraction patterns (not shown here) only showed sharp anatase rings. The absence of a crystalline WO_3 phase in these diffraction patterns indicates that coupled WO_3 species were present either in an amorphous state or as nanocrystallites, but not in an amount that was detectable by the diffraction methods. Notably, after annealing, the two film types still possessed the same XRD pattern shown in Fig. 4 (pattern a) without the appearance of any new peaks of impurity phases.

Fig. 4 shows that the as-deposited films (W/Ti ratio=0.55) only yielded broad XRD peaks with a full width greater than 15° at half the maximum (see pattern b). TEM analysis revealed that selected area diffraction patterns taken from a thin foil of the films only contained halos (micrographs not shown); it was not possible to observe any lattice fringe from the high-resolution TEM micrographs recorded from any region or orientation of the foils. All of these results suggest that the films with sufficient tungsten species became amorphous. After annealing, the broad peak was converted into two sets of sharp peaks, as identified in pattern c of Fig. 4: one was from the anatase matrix (JCPDS 21-1272), and the other was due to the formation of a new phase, Na_2WO_4 (JCPDS 70-1040). Na_2WO_4 , a water-soluble substance, was removed from the samples upon water immersion. As a consequence, the resultant films only contained the anatase phase (Fig. 4, pattern d), which is consistent with a dramatic decay of the atomic concentration of tungsten and a complete disappearance of the segregated sodium observed by the RBS and XPS.

SEM imaging revealed that the as-deposited TiO_2 films had a uniform grain structure, and the grain sizes were refined by the incorporation of the tungsten species. Moreover, the initial amount of tungsten was a key factor that decided the final microstructures and surface morphologies of the annealed films. These findings can be clearly seen by comparing the SEM and TEM micrographs shown in Figs. 5–8. Fig. 5A demonstrates that the as-deposited films with a low tungsten content (W/Ti ratio=0.08) yielded homogeneous morphologies in the top-view SEM images. After annealing, grains of the film matrixes approximately doubled in average size from 16 to 28 nm, along with the formation of a scattered dispersion of large precipitates (with sizes typically of 200 nm across) on the film surfaces (see Fig. 5B). As visible in the micrograph, the crystallites, isolated on the surface, were characteristically regular with faceting and symmetric morphology that suggested a single-crystal nature. Consistently, TEM micrographs of the cross-sectional

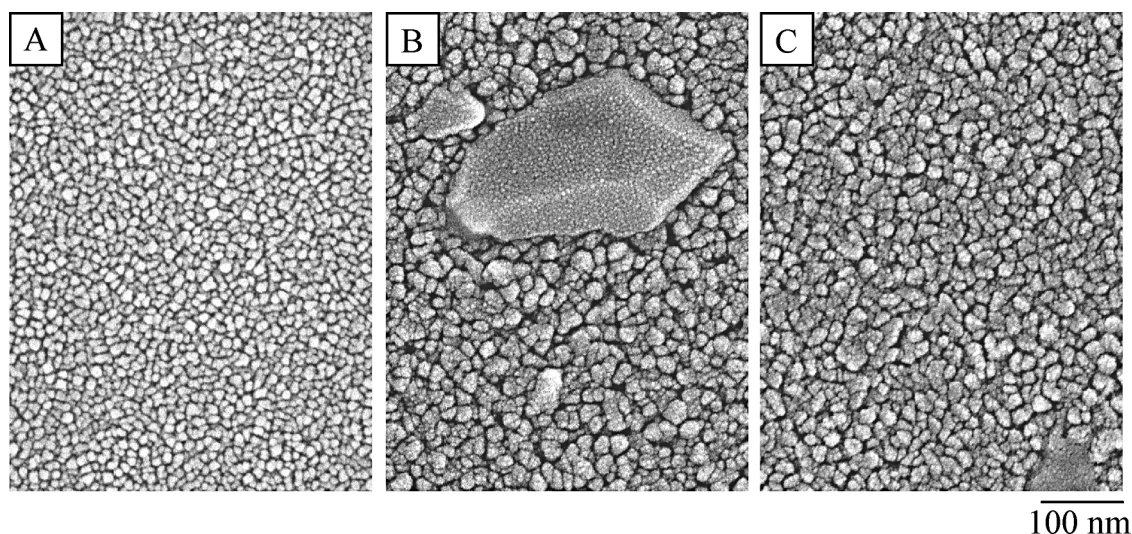


Fig. 5. Top-view SEM micrographs showing variations of surface morphologies of the lightly-doped (W/Ti = 0.08) pristine TiO_2 samples (A) as a function of the sequential treatments of annealing (B) and washing (C).

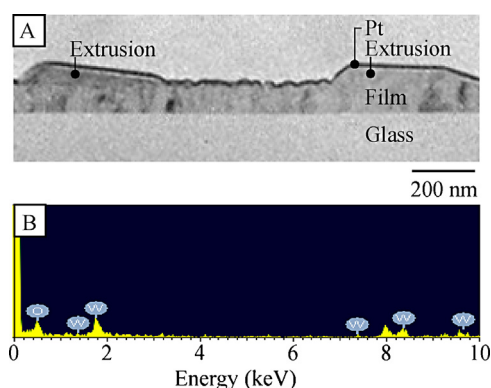


Fig. 6. Cross-sectional TEM micrograph (A), along with the recorded EDX spectrum (B), revealing the presence of WO_3 extrusions on the lightly doped (W/Ti = 0.08) TiO_2 samples after annealing. The peak at ~8 keV was due to a thin Pt coating needed for focused-ion-beam sample preparation.

samples revealed that the crystallites indeed appeared as extrusions with sizes also of ~200 nm on the film surfaces (see Fig. 6A). EDX spectra recorded from these crystallites *in-situ* only contained tungsten and oxygen signals (Fig. 6B), suggesting that they were tungsten oxide (WO_3). As demonstrated in Fig. 5C, the isolated WO_3 crystallites were loosely adhered to the underlying films, and thus readily detached from the films during water immersion or sample handling, leaving the films in only the anatase phase.

As revealed by the top-view SEM micrographs in Fig. 7A–C, the films with the highest tungsten content (W/Ti ratio = 0.55) displayed a completely different microstructural modification after the two-step processing. Fig. 7A indicates that the as-deposited films yielded a uniform, speckled surface morphology. Fig. 7B shows that annealing caused a conversion of the uniform surface into an uneven morphology that was characterized by dramatically enlarged, coarse grains. The TEM micrograph in Fig. 8A, obtained from a cross section of the sample in Fig. 7B, clearly reveals that the film surface was covered by a segregation layer, also manifesting itself as an uneven, granular surface morphology in Fig. 7B. EDX spectra, recorded from the segregation layer using a 2-nm-sized electron beam, only contained W, Na, and O signals (see Fig. 8B). This complementary result reinforces the finding of XRD that the segregation layer indeed was Na_2WO_4 . Upon water treatment, the

Na_2WO_4 surface layer, together with the Na_2WO_4 within the sample, instantly dissolved in water, corresponding to a reduction in the concentrations of sodium and tungsten across the films observed by the depth-profiling XPS in Fig. 3. According to Fig. 7C, the resultant films appeared to contain an aggregation of nanocrystallites with a sponge-like microstructure—a configuration completely different from the dense microstructures of the TiO_2 and low-tungsten-content films shown in Fig. 5C.

3.3. Catalyst performance

This research has presented a new method to fabricate a featured anatase-based film by thermally processing WO_3 -containing TiO_2 film by means of the synergetic effect of the WO_3 on the sodium in the underlying glass. Fig. 9A shows the evolution of water contact angles for the WO_3 -containing films before (plot a) and after (plot b) the two-step processing; for comparison, the experimental results obtained from an undoped anatase film are displayed in plot c. All the films were coated with an OTS-SAM [$\text{CH}_3(\text{CH}_2)_{17}\text{Si}-$] prior to ultraviolet illumination. According to Fig. 9A, the initial contact angles of all the monolayer-coated samples were as high as 110° because their surfaces were terminated by nonpolar methyl groups [38]. Previous studies have shown that the decomposition of monolayers' alkyl chains by photocatalytic oxidation upon ultraviolet illumination leads to a gradual decrease in water contact angle [33,34]. Therefore, photoactivity of the catalytic films can be evaluated by monitoring the alteration of the water contact angles, shown in Fig. 9A.

Fig. 9A reveals that even after a long period of light illumination for 6 h, the water contact angle of the pristine film was still greater than 100° (see plot a), indicating that the WO_3 -containing amorphous film lacked the photoactivity to dissociate the alkyl-siloxane monolayer. This finding is not surprising, as it is commonly observed for other TiO_2 -based films/nanostructures with an amorphous structure [37,39]. However, when treated by annealing and water washing, the degradation of the hydrocarbon molecular chains through photoactivity significantly improved (see Fig. 9A, plot b). Anatase is generally regarded as a better photocatalyst than rutile, mainly because its thermodynamically stable (1 0 1) surface yields a higher reduction and oxidation power than the rutile's thermodynamically stable (1 1 0) surface [40]. The films developed here are even better than general anatase films, the well-known

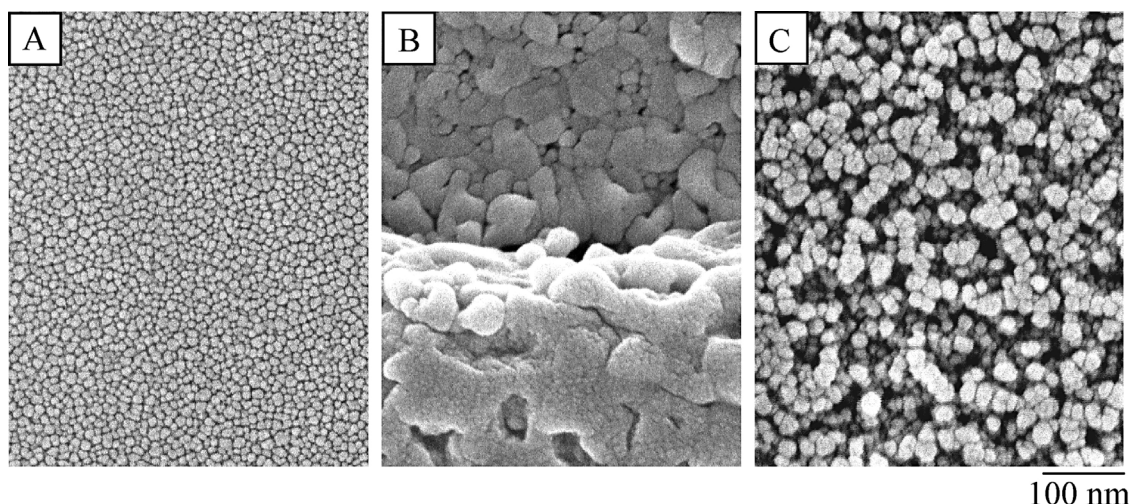


Fig. 7. Top-view SEM micrographs showing variations of surface morphologies of the heavily-doped (W/Ti=0.55) pristine TiO₂ samples (A) as a function of the sequential treatments of annealing (B) and washing (C).

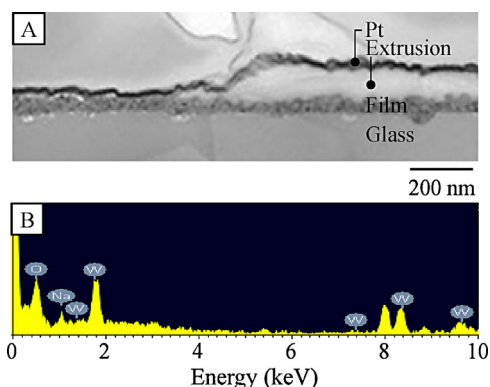


Fig. 8. Cross-sectional TEM micrograph (A), along with the recorded EDX spectrum (B), revealing the formation of Na₂WO₄ for the heavily doped (W/Ti=0.55) TiO₂ samples after annealing. The peak at ~8 keV was due to a thin Pt coating for focused-ion-beam sample preparation.

effective photocatalysts, at degrading the hydrocarbon molecular chains; they have a much faster reduction rate and lower values of water contact angle (compare plots b and c in Fig. 9A).

The films were also tested by many cycles of ultraviolet illumination (1 day) and dark-room storage (1 day), which allowed us to evaluate their photoinduced hydrophilicity properties and persistence in the dark. As shown in Fig. 9B, although initially having a fine wetting property with water contact angles of less than 5°, the undoped anatase TiO₂ films began to lose hydrophilicity after 30 days of testing, probably due to the loss of active sites by the accumulation of carbonaceous contamination on the surface [41,42]. In contrast, the WO₃-derived films had excellent, durable superhydrophilicity with water contact angles of less than 5° throughout the 3-month period of test.

3.4. Status of the dopant species and phase-transition sequence of sodium tungstates

Numerous studies have found that two kinds of tungsten species, lattice doping tungsten and WO₃, can be coupled into the bulk of TiO₂ [43–45]. When the tungsten content is low, most of the tungsten species stay in the lattice sites substituting the titanium ions. The amount of the lattice doping tungsten increases to a saturation point, after which the additional tungsten species form WO₃ compounds. A wide range of the saturation concentrations has been

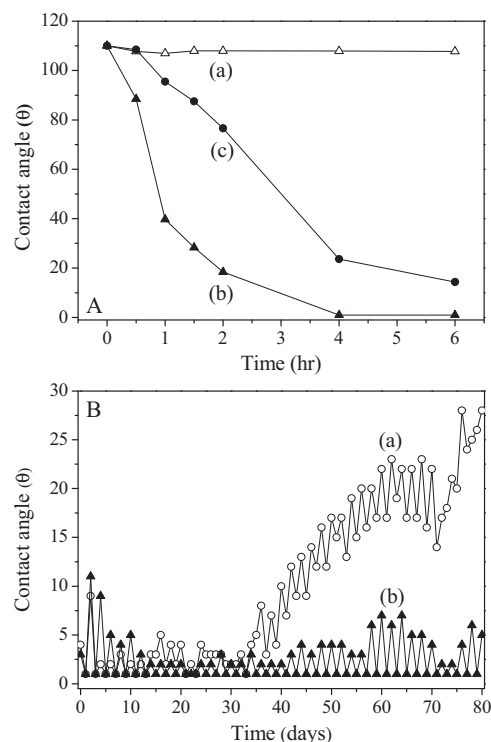


Fig. 9. (A) Evolution of water contact angles for the heavily doped film before (a) and after (b) the two-step processing, along with the plot obtained from the undoped anatase film (c). All films were coated with an SAM prior to test. (B) Evolution of water contact angles during cycling test (ultraviolet illumination and dark-room storage) of the undoped TiO₂ (a) and heavily doped (b) TiO₂ films after the two-step processing.

reported, all of which appear to be primarily dependent on the fabrication method. For example, 20 at% of tungsten is incorporated into the substitutional sites of TiO₂ nanocomposites formed by a microemulsion method [43], while a very small amount of tungsten reagents (less than 1 wt%) loaded into hydrothermally synthesized TiO₂-WO₃ photocatalysts has already formed crystalline WO₃ [44]. Based on the experimental data from RBS, XPS, and XRD, it is very likely that all the tungsten-containing film types examined here also contained the two kinds of tungsten species in different proportions. After the two-step processing, the WO₃ compound was

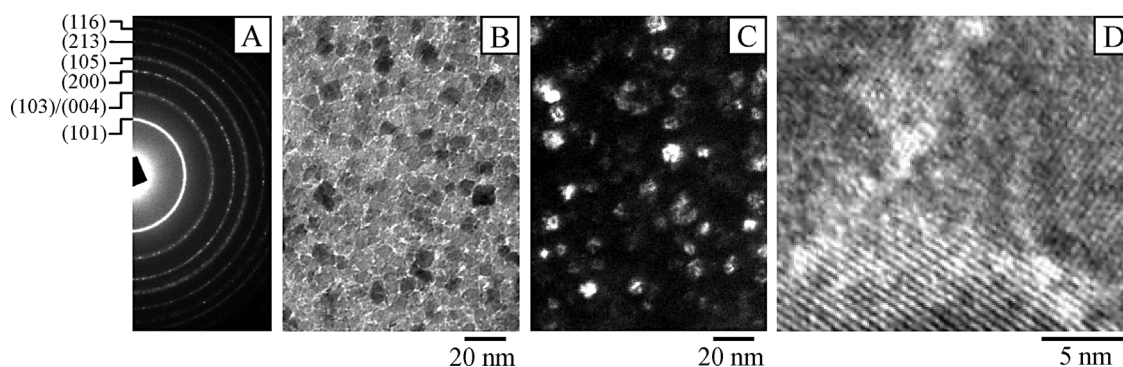


Fig. 10. Selected area electron diffraction pattern (A) and bright-field (B), dark-field (C), and high-resolution (D) TEM micrographs for the heavily doped (W/Ti ratio = 0.55) TiO_2 films after the two-step processing.

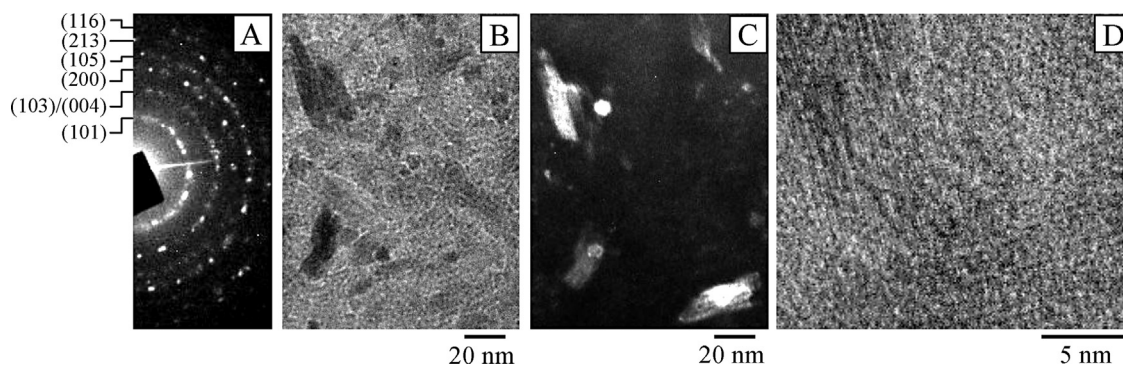


Fig. 11. Selected area electron diffraction pattern (A) and bright-field (B), dark-field (C), and high-resolution (D) TEM micrographs for the undoped TiO_2 films after the two-step processing.

totally driven out of the TiO_2 matrixes, leaving behind only the lattice doping tungsten. According to the RBS analysis in Fig. 2 and the TEM study presented later, the concentrations of the residual tungsten were approximately the same for all of the film types, ~ 0.07 in terms of the W/Ti ratio.

According to the TiO_2 - WO_3 binary phase diagram [46], WO_3 was immiscible with TiO_2 at temperatures below the eutectic temperature (1233°C). Therefore, when performing thin-film deposition by poisoned-mode sputtering of the Ti-W alloy targets, the sputtered tungsten species generally existed heterogeneously as WO_3 within the TiO_2 film matrix. Previous studies have found that TiO_2 (or TiO)- WO_3 composite films sputter deposited onto inert substrates such as Si wafers or Al_2O_3 plates require high-temperature (e.g., 700°C) and prolonged (≥ 10 h) annealing in order for the WO_3 to segregate completely on the film's surface as big clumps of crystallites (average width of $1\text{ }\mu\text{m}$) [47]. In this research, the WO_3 incorporated within the low-tungsten-content films (W/Ti ratio = 0.08) indeed was expelled to the surface as isolated WO_3 crystallites by annealing and subsequently removed by water immersion or sample handling (Fig. 5). We measured their ability to dissociate an OTS-SAM by the method presented in Fig. 9A. The water contact angle of the SAM-coated films was reduced from 105° to only 60° after light exposure for 6 hr, indicating that their photocatalytic activity was inferior to that of the pure- TiO_2 anatase films.

In the films with appreciable WO_3 after annealing ($550^\circ\text{C}/1$ h or 30 min), the incorporated WO_3 was not simply expelled out to the surface; instead, it mutually attracted sodium from within glass, resulting in the segregation of WO_3 and sodium via the formation of Na_2WO_4 . Previous studies have shown that the strong affinity and chemical reactivity between WO_3 and Na_2O (or sodium-based salts) could result in the formation of various sodium tungstates with different stoichiometries, such as $\text{Na}_2\text{W}_4\text{O}_{13}$ and

$\text{Na}_2\text{W}_2\text{O}_7$ during thermal treatments [29,48,49]. To further clarify the phase-transition behavior here, the WO_3 -incorporated TiO_2 films were air-annealed at 550°C for various periods of time ranging from a few minutes to 120 min, and the 'time-resolved' XRD patterns revealed a phase transition sequence of the sodium tungstates that ultimately formed Na_2WO_4 . From this analysis, it is believed that Na_2WO_4 was formed by the following chemical reaction sequence: (a) $\text{Na}_2\text{W}_4\text{O}_{13} + \text{Na}_2\text{O} \rightarrow 2\text{Na}_2\text{W}_2\text{O}_7$; (b) $\text{Na}_2\text{W}_2\text{O}_7 + \text{Na}_2\text{O} \rightarrow 2\text{Na}_2\text{WO}_4$ (see Supplementary data for details of the XRD analysis of the phase-transition behavior).

3.5. Origins of the improved photoactivity and porosity deduction

Selected area electron diffraction patterns for all the film types after the two-step treatment highlighted a polycrystalline layer featuring only anatase crystals. The absence of diffraction rings of WO_3 suggests that the residual tungsten observed in Fig. 2 was indeed entirely located in the lattice sites. An example of electron diffraction patterns is presented in Fig. 10A—the films derived from the WO_3 -containing films (W/Ti ratio = 0.55). The bright-field image in Fig. 10B, along with the dark-field image recorded by placing an objective aperture on the (1 0 1) ring (Fig. 10C), shows that this film type possessed regular, equiaxed crystallites with an average grain size of ca. 10 nm. The high-resolution TEM micrograph, shown in Fig. 10D, is dominated by anatase lattice fringes of typically ~ 10 nm across. It has been reported that coupled WO_3 (or other metal oxide) segregates into the grain boundaries of titania after annealing [28]. In the present study, however, precipitation of WO_3 at the grain boundaries was not detected by the high-resolution TEM analysis. Instead, pores with sizes of typically 2 nm existed as 'bright spots' in the regions between adjacent TiO_2 grains.

Fig. 11A displays an electron diffraction pattern of a treated, pure TiO₂ film, taken by a TEM setup the same as that of Fig. 10A. The diffraction rings were identified all from reflections of anatase crystallographic planes; their spotty feature suggests that grain sizes of the undoped anatase films were coarser than those of the WO₃-derived TiO₂ films (compare Fig. 10A). We used bright-field and dark-field techniques to illustrate their anatase crystallites, and the resulting micrographs, displayed respectively in Fig. 11B and C, reveal an average grain size of ca. 30 nm, considerably larger than that of the porous films in Fig. 10. The elongated crystallites, signifying a high density of crystallographic defects, were also very different from the regular, equiaxed crystallites of the porous films. Moreover, high-resolution TEM imaging of the reference films of pure TiO₂ only showed a dense and compact lattice structure that prevented the detection of pores (see Fig. 11D). Notably, the direct observation of the grain sizes by TEM imaging presented above was consistent with that obtained from the XRD analysis in Fig. 4 (patterns a and d) by the Scherrer's equation [50]. The average grain sizes of the porous and dense TiO₂ films were 13 and 32 nm, respectively.

We estimated the porosities of the WO₃-derived films based on the processing-induced changes in the film thicknesses and the areal densities of the constituting components (TiO₂ and WO₃), shown in Figs. 1 and 2. Cross-sectional TEM (or SEM) imaging (micrographs not shown here) revealed that thickness of the as-deposited films was 100 nm, and the magnitude of thickness reduction depended on thermal budget of the annealing. For example, the final thicknesses of the films after 550 °C annealing for 1 h and 30 min were 64 and 72 nm, respectively. RBS analysis revealed that areal densities of the TiO₂ matrix and the incorporated WO₃ (deducting the substituting W species), denoted AD_{Ti} and AD_W, were 3.26×10^{17} and 1.50×10^{17} molecules/cm², respectively. After treatment, the former remained unchanged, while the later was reduced to nil. Based on these findings, we assume the following: (a) the removal of the incorporated WO₃ left behind pores within the film matrix; (b) shrinkage of the pores caused the initial film thickness ($t_i = 100$ nm) to reduce to a value denoted as t_f ; (c) the molecular densities of the anatase TiO₂ and WO₃ substances in the film, denoted MD_{Ti} and MD_W, respectively, were the same as the bulk values, and were derived from their mass densities, i.e., 3.9 g/cm³ (TiO₂) and 7.2 g/cm³ (WO₃) [51], as 3.19×10^{22} and 1.86×10^{22} molecules/cm³, respectively. Thus, the initial volume of the pores produced upon the removal of WO₃, denoted as V_i , can be calculated by the equation, $V_i = (AD_W)/t_i \cdot (MD_W)$, which was 0.806 cm³. Similar calculation showed that the volume of the TiO₂ matrix (V_{Ti}), which remained unchanged after the treatments, was 1.022 cm³. Denoting the area of the films and the final volume of the pores as A and V_{pore} , respectively, the volumes of the untreated and treated films can be respectively expressed in unit of cm³ by the equations: (a) $t_i \cdot A = 1.022 + 0.806$ and (b) $t_f \cdot A = 1.022 + V_{pore}$. Based on this set of data, the porosities of the films ($V_{pore}/V_{Ti} + V_{pore}$) annealed for 60 and 30 min were 15% and 30%, respectively.

In sum, photoactivity of the WO₃-derived films is considerably better than that of the undoped anatase films. This is attributed to the porous structure, which leads to a significantly larger surface area that increases the photoactivity. Additionally, the inhibition of crystal growth and the diminishment of crystallographic defects, generally thought of as photoactivity-enhancers [19,52], are also deemed to be contributing factors.

4. Conclusions

TiO₂ thin films doped with a widely ranging amount of tungsten species (W/Ti atomic ratios up to 0.55) were deposited by high-pressure sputtering on soda-lime glass substrates, and the effect

of a two-step processing (annealing and water washing) on the transformations of their microstructures/phases was investigated, using undoped TiO₂ films as a reference. All the films were identified to have the same concentration of lattice doping tungsten (W/Ti atomic ratio = 0.07), and the rest of tungsten existed as WO₃ species. During annealing, only the WO₃ species were expelled, which existed as faceted WO₃ single-crystal precipitates on the film surfaces (lightly-doped films), or as water-soluble Na₂WO₄ across the films by the mutual chemical reaction of WO₃ and the glass's sodium (heavily doped films).

The reference films were immune to thermally induced diffusion of sodium and exhibited a dense anatase matrix comprising irregular grains of sizes exceeding 30 nm. In contrast, the doped TiO₂ films only with appreciable WO₃ were significantly impacted by the glass's sodium and ultimately exhibited a mesoporous anatase matrix with the catalytic-favoring microstructure of regular and refined (10-nm-sized) grains. The mesoporous films showed much better photoactivity than the undoped anatase films at degrading a hydrocarbon layer and giving a long-last, durable super-wetting surface. The result is quite different from the previous finding that the glass's sodium is a contaminant that reduces photocatalytic activity of TiO₂ films. It should be noted that photoactivity of the films could be further improved by the manipulation of their porosities through the controls of the WO₃ dopant concentration and thermal budget of annealing. This opens up a possibility of using the sputtering process, among the commonly used template-directing sol-gel methods, to synthesize mesoporous anatase films with exceptionally durable photocatalytic activity, involving the novel matrix of TiO₂ and transition-metal and sodium oxides (not necessarily tungsten oxide or sodium from glass) through a simple annealing process.

Acknowledgements

The work was supported by the National Science Council, Taiwan and H.P.B. Optoelectronics Co., under grant number NSC100-2622-E-035-015-CC2. Prof. C.P. Liu and Dr. H. Niu are acknowledged for assistance of TEM and RBS analyses, respectively. We are also grateful to National Synchrotron Radiation Research Center and Precision Instrument Support Center of Feng Chia University for providing facilities.

Appendix A. Supplementary data

Supplementary data associated with this article can be found, in the online version, at <http://dx.doi.org/10.1016/j.apcatb.2013.12.017>.

References

- [1] S. Kwon, M. Fan, A.T. Cooper, H.Q. Yang, Crit. Rev. Environ. Control 38 (2008) 197–226.
- [2] H.J. Zhang, G.H. Chen, D.W. Bahnemann, J. Mater. Chem. 19 (2009) 5089–5121.
- [3] R. Wang, K. Hashimoto, A. Fujishima, M. Chikuni, E. Kojima, A.A. Kitamura, M. Shimohigoshi, T. Watanabe, Nature 388 (1997) 431–432.
- [4] A. Fujishima, X.T. Zhang, C. R. Chim. 9 (2006) 750–760.
- [5] R. Scotti, M. D'Arienzo, F. Morazzoni, I.R. Bellobono, Appl. Catal. B 88 (2009) 323–330.
- [6] J. Dostanic, B. Grbic, N. Radic, S. Stojadinovic, R. Vasilic, Z. Vukovic, Appl. Surf. Sci. 274 (2013) 321–327.
- [7] F. Bosc, A. Ayrault, N. Keller, V. Keller, J. Sol. Energy Eng. 130 (2008) 041006-1–041006-5.
- [8] Yu. Gnatyuk, N. Smirnova, O. Korduban, A. Eremenk, Surf. Interface Anal. 42 (2010) 1276–1280.
- [9] M.C. Fuentes, G.J.A.A. Soler-Illia, Chem. Mater. 18 (2006) 2109–2117.
- [10] K. Ho, J.C. Yu, S.C. Lee, Appl. Catal. B 73 (2007) 135–143.
- [11] J. Zhu, J. Yang, Z.F. Bian, J. Ren, Y.M. Liu, Y. Cao, H.X. Li, H.Y. He, K.N. Fan, Appl. Catal. B 76 (2007) 82–91.
- [12] T. Matsunaga, H. Yamaoka, S. Ohtani, Y. Harada, T. Fujii, T. Ishikawa, Appl. Catal. A 351 (2008) 231–238.

- [13] R. Fateh, R. Dillert, D. Bahnemann, *Langmuir* 29 (2013) 3730–3739.
- [14] X.C. Wang, J.C. Yu, Y.L. Chen, L. Wu, X.Z. Fu, *Environ. Sci. Technol.* 40 (2006) 2369–2374.
- [15] Y.M. Chen, F. Chen, J.L. Zhang, *Appl. Surf. Sci.* 255 (2009) 6290–6296.
- [16] B. Braconnier, C.A. Paez, S. Lambert, C. Alie, C. Henrist, D. Poelman, J.P. Pirard, R. Rudi, B. Heinrichs, *Microporous Mesoporous Mater.* 122 (2009) 247–254.
- [17] H. Tada, M. Tanaka, *Langmuir* 13 (1997) 360–364.
- [18] Y. Paz, A.J. Heller, *Mater. Res.* 12 (1997) 2759–2766.
- [19] H.J. Nam, T. Amemiya, M. Murabayashi, K. Itoh, *J. Phys. Chem. B* 108 (2004) 8254–8259.
- [20] N.M. Ghazzal, N. Chaoui, E. Aubry, A. Koch, D.J. Robert, *Photochem. Photobiol. A* 215 (2010) 11–16.
- [21] J. Krysa, P. Novotna, S. Kment, A. Mills, *J. Photochem. Photobiol. A* 222 (2011) 81–86.
- [22] U. Joost, R. Parna, M. Leminen, K. Utt, I. Kink, M. Visnapuu, V. Kisand, *Phys. Status Solidi A* 210 (2013) 1201–1212.
- [23] J. Yu, X. Zhao, *Mater. Res. Bull.* 36 (2001) 97–107.
- [24] J. Zita, J. Maixner, J.J. Krysa, *Photochem. Photobiol. A* 216 (2010) 194–200.
- [25] E. Aubry, J. Lambert, V. Demange, A. Billard, *Surf. Coat. Technol.* 206 (2012) 4999–5005.
- [26] Y.T. Kwon, K.Y. Song, W.I. Lee, G.J. Choi, Y.R. Do, *J. Catal.* 191 (2000) 192–199.
- [27] M. Fernandez-Garcia, A. Martinez-Arias, A. Fuente, J.C. Conesa, *J. Phys. Chem. B* 109 (2005) 6075–6083.
- [28] D.S. Kim, J.H. Yang, S. Balaji, H.J. Cho, M.K. Kim, D.U. Kang, Y. Djoued, Y.U. Kwon, *CrystEngComm* 11 (2009) 1621–1629.
- [29] G.S. Chen, J.H. Chen, J.N. Kuo, Y.Y.W. Chen, H. Niu, *Mater. Lett.* 109 (2013) 217–220.
- [30] D.L. Smith, *Thin-Film Deposition: Principles and Practice*, McGraw-Hill, Inc., New York, 1995.
- [31] G.S. Chen, C.C. Lee, H. Niu, W. Huang, R. Jann, T. Schütte, *Thin Solid Films* 516 (2008) 8473–8478.
- [32] S.T. Chen, G.S. Chen, *Langmuir* 27 (2011) 12143–12148.
- [33] J.P. Lee, H.K. Kim, C.R. Park, G. Park, H.T. Kwak, S.M. Koo, M.M. Sung, *J. Phys. Chem B* 107 (2003) 8997–9002.
- [34] X.T. Zhang, M. Jin, Z.Y. Liu, D.A. Tryk, S. Nishimoto, T. Murakami, A. Fujishima, *J. Phys. Chem. C* 111 (2007) 14521–14529.
- [35] D. Liu, S.K. Dew, M.J. Brett, T. Smy, W. Tsai, *J. App. Phys.* 75 (1994) 8114–8120.
- [36] Z.W. Zhao, B.K. Tay, *J. Appl. Phys.* 101 (2007) 013505-1–013505-5.
- [37] T. Tolke, A. Kriltz, A. Rechtenbach, *Thin Solid Films* 518 (2010) 4242–4246.
- [38] E. Tyrode, J.F.D. Liljeblad, *J. Phys. Chem. C* 117 (2013) 1780–1790.
- [39] J.G. Yu, G.P. Dai, B. Cheng, *J. Phys. Chem. C* 114 (2010) 19378–19385.
- [40] A.Y. Ahmed, T.A. Kandiel, T. Oekermann, D. Bahnemann, *J. Phys. Chem. Lett.* 2 (2011) 2461–2465.
- [41] C.Y. Wang, S.H. Pang, Q. Lu, T.C. Ma, P.W. Wang, *Mater. Chem. Phys.* 125 (2011) 281–285.
- [42] N. Ishida, D. Fujita, *J. Vac. Sci. Technol. A* 30 (2012) 051402-1–051402-5.
- [43] A. Fuente, M.D. Hernandez-Alonso, A.J. Maira, A. Martinez-Arias, M. Fernandez-Garcia, J.C. Conesa, J. Soria, G. Munuera, *J. Catal.* 212 (2002) 1–9.
- [44] V. Puddu, R. Mokaya, G.L. Puma, *Chem. Commun.* 45 (2007) 4747–4751.
- [45] S.A.K. Leghari, S. Sajjad, F. Chen, J. Zhang, *Chem. Eng. J. (Amsterdam Neth.)* 166 (2011) 906–915.
- [46] L.L.Y. Chang, M.G., Scroger, B. Philips, in: E.M. Levin, H. F. McMurdie (Eds.), *Phase Diagram for Ceramists*, Vol. III, The American Ceramic Society, Westerville, Ohio, 1975, p. 171.
- [47] M. Ferroni, V. Guidi, G. Martinelli, E. Comini, G. Sberveglieri, D. Boscarino, G. Della Mea, *J. Appl. Phys.* 88 (2000) 1097–1103.
- [48] S. Oishi, N. Endo, M. Itoh, *J. Crys. Growth* 229 (2001) 477–481.
- [49] C.Y. Kim, S.H. Huh, D.H. Riu, *Mater. Chem. Phys.* 116 (2009) 527–531.
- [50] B.D. Cullity, S.R. Stock, *Elements of X-Ray Diffraction*, third ed, Prentice Hall, New Jersey, 2001.
- [51] D.L. Lide, *CRC Handbook of Chemistry and Physics*, 90th ed. (2009–2010), CRC Press, Taylor & Francis Group, New York, 2013, pp. 4–96–4–97.
- [52] H. Choi, E. Stathatos, D.D. Dionysiou, *Top. Catal.* 44 (2007) 513–521.